This is a post-peer-review, pre-copyedit version of an article published in Continuum Mech. Thermodyn. The final authenticated version is available online at:
http://dx.doi.org/10.1007/s00161-019-00850-7

Piotr J. Ziółkowski · **Tomasz Ochrymiuk** · **Victor A. Eremeyev**

Adaptation of the arbitrary Lagrange–Euler approach to fluid–solid interaction on an example of high velocity flow over thin platelet

Abstract The aim of this study is to analyse the behaviour of a thin plate with air flow velocities of 0.3–0.9 Ma. Data from the experiment and numerical tools were used for the analysis. For fluid–solid interaction calculations, the arbitrary Lagrange–Euler approach was used. The results of the measurements are twofold. The first one is the measurement of the flow before and after vibrating plate, i.e. pure flow plate, and the second consists in measuring the characteristics of vibration of the plate. The character of the vibration was measured with an oscilloscope, and then the results were subjected to FFT analysis to determine the natural and flow induced vibrations. For numerical calculations example, the velocity of 0.7 Ma was selected. The deflections of the platelet under the influence of airflow were obtained. The trace of the friction layer that forms the boundary between the flow from the platelet and the separation formed behind the platelet.

Keywords Fluid–solid interaction · Arbitrary Lagrangian–Eulerian (ALE) description · Computational solid dynamics (CSD) · Computational fluid dynamics (CFD)

1 Introduction

Studies on fluid–solid interactions are interdisciplinary, combining aerodynamic, inertial and elastic forces in such a way that the structure and the flow around it interact with each other. Such mutual relationships can cause vibration damping, maintenance of a specific vibration amplitude or an increase in vibration amplitude. Maintaining or increasing the vibration amplitude is defined as self-excited vibrations or flatter. There are many definitions of a flatter. Flatter can be defined as nonlinear in nature unstable and self-excited vibrations of a flexible body in a flow as a result of continuous interaction between the flow and a vibrating structure. Flatter appears above a certain flow velocity causes an increase in vibration amplitude and can cause structural damage.

The phenomena accompanying the interaction of liquid and solid are of great importance in aeronautics, power engineering (in steam and gas turbines), in construction, especially in the case of slender structures such as bridges, towers and masts. For example, in the construction industry, the flow velocity of the air in

P. J. Ziółkowski (✉) · T. Ochrymiuk
Institute of Fluid Flow Machinery, Polish Academy of Sciences, Gdańsk, Poland
E-mail: pjziolkowski@imp.gda.pl

P. J. Ziółkowski · V. A. Eremeyev
Faculty of Civil and Environmental Engineering, Gdańsk University of Technology, Gdańsk, Poland

V. A. Eremeyev
Southern Federal University, Rostov-on-Don, Russia

Poland is relatively low. Speed 33.6 m/s (≈ 0.097 Ma) is considered as the lower limit of wind speed, which is considered a hurricane, i.e. 12° on the Beaufort scale according to World Meteorological Organization [1], but this speed occurs rarely in Polish conditions. According to Lorenc [2], gusts of wind with speeds exceeding ≥ 33 m/s in the years 1971–2005 for Bielsko-Biała occurred in 40 months out of 420 observed. When creating models for the flow of building structures, the flow can be treated as an incompressible flow; on the other hand, in aeronautics and power engineering, where the velocity of the factor reaches and even exceeds the speed of sound (≈ 340 m/s), the compressibility must be taken into account. The limit value of the factor velocity at which the compressibility of gases should be taken into account is 0.4 of the sound velocity [3], because in this case the pressure differences are so significant that the effect of gas compressibility on the flow becomes significant. The change of gas density is accompanied by the change of its temperature, apart from the issues of fluid dynamics, thermodynamic issues should be taken into account.

The aim of this study is to compare the experiment of thin plate flow in a wind tunnel with Fluid–Solid Interactions (FSI) calculations using the arbitrary Lagrange–Euler (ALE) approach.

FSI analyses can be used to verify the operating comfort of bridge structures [4], when interpreting non-stationary forces and pressures acting on slender structures [5], for flow-solid analysis when large temperature gradients appear on the flow side, it is also very important in engineering, e.g. when testing the material strength of the guide vane 1-st turbine of the PZL-10W engine compressor [6], when brittle bodies, e.g. glass, are stressed [7], when testing non-stationary forces acting on structural elements in turbines, e.g. a thermometer for measuring the temperature of flowing steam [8], a Y-junction designed to combine two streams of water vapour into one [9], degradation rate of the shut-off valve in 200 MW of the steam power plant unit [10]. Ochrymiuk [11] considered the efficiency of the cooling layer that occurs in the cooling system of gas turbine blades. It is worth noting that FSI tools are also applicable in medicine, see, e.g. Czechowicz et al. [12]. In [12] have been investigated the wall shear stress generated by the pulsate flow of the blood, and blood pressure in the cardiovascular system.

As can be seen from the above examples, knowledge of the phenomena accompanying the exchange of mass, momentum and energy occurring on the surface between a fluid and a solid is essential in many fields of engineering. Moreover, the field is multidisciplinary and multiscallability. The multiscale nature of FSI phenomena is well illustrated paper by Badur et al. [13], where the figure schematically shows the location of some phenomena concerning the interaction of a fluid with a solid body. In [13], the authors emphasized the phenomena occurring in the contact layer between solid and liquid on a micro- and nano-scale. On this layer, a large variety of nano-scale phenomena are present, such as Navier's slip velocity [14], the Reynolds transpiration law [15] and phenomena called "jumps" relating to temperature, pressure, factor concentration or electrical potential. Attempts to develop the thermodynamics of the continuum with these phenomena looking for their basis in experiments can be found in [14,16–19].

However, the main interest of this work is macro-scale phenomena, i.e. the aforementioned flatter, vortex paths behind the plate, air stream separation or plate vibrations in the flow. The paper is organized as follows. First, in Sect. 2, we introduce the arbitrary Lagrangian–Eulerian approach in order to capture advantages of both Lagrangian and Eulerian approaches known in continuum mechanics. In Sect. 3, we discuss the experimental results on oscillations of an elastic platelet. Finally, in Sect. 4, we present the numerical results and compare them with observed experimental behaviour.

2 Arbitrary Lagrangian–Eulerian approach to fluid–solid interaction

ıngian description and Eulerian description are two classic descriptions of motion, which are widely used ıtinuum mechanics algorithms. Computational solid dynamics (CSD) mainly makes use of Lagrangian ithms, while Computational Fluid Dynamics (CFD) employs mainly Eulerian algorithms. Each node of utational grid follows the associated material particle during motion in Lagrangian algorithms, which s one to easily track free surfaces and interfaces between different materials. However, it is unable to large distortions. On the other hand, in Eulerian algorithms, the computational mesh is fixed and the ıuum moves with respect to the grid and large distortions can be handled relatively easily, but generally he expense of precise interface definition and the resolution of flow details [20].

ı the ALE description, three options occurs: The nodes of the computational mesh can be moved with ontinuum in normal Lagrangian manner, can be held fixed in Eulerian manner, or, can be moved in specified arbitrarily specified way providing additional flexibility and accuracy. The ability to select the ary motion of the calculation grid is the essence of the arbitrary Lagrangian–Eulerian formulation [21].

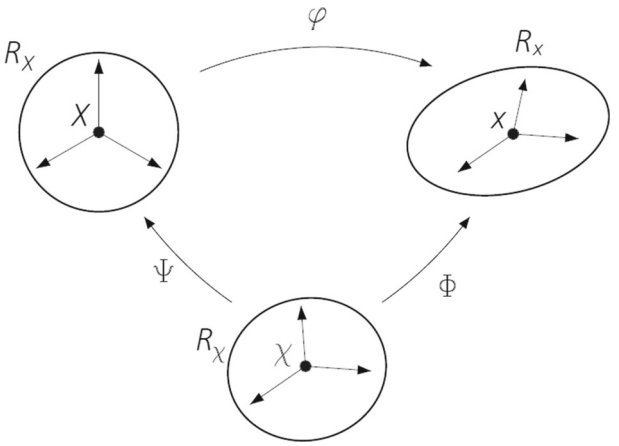

Fig. 1 Material, spatial and referential domains in motion

Because of the shortcomings of Lagrange's and Euler's description, the arbitrary Lagrangian–Eulerian (ALE) description has been developed, in which the advantages of both descriptions have been exploited by combining them. In the text below, the ALE description is presented as a generalization of the classical Lagrangian and Eulerian description of motion.

2.1 Description of the arbitrary Lagrangian–Eulerian kinematics

Let us consider two domains (Fig. 1), which are commonly used in continuum mechanics. The material domain is denoted as $R_X \subset \mathbb{R}^{n_{\mathrm{sd}}}$, with n_{sd} spatial dimensions, consisting of material particles $\boldsymbol{X}$, and the spatial domain R_x, composed of spatial points $\boldsymbol{x}$ and additionally a third domain R_χ is introduced, which serves as a reference configuration where reference coordinates $\boldsymbol{\chi}$ are utilized to identify the mesh points.

The Lagrangian viewpoint consists of the following: the observation of the material particles of the continuum in their motion. The material coordinates, $\boldsymbol{X}$, allow us to identify the configuration, R_x . The motion of the material points relates the material coordinates, $\boldsymbol{X}$, to the spatial ones, $\boldsymbol{x}$. It is achieved by introducing a following mapping $\boldsymbol{\varphi}$:

$$\begin{aligned} &\boldsymbol{\varphi}: R_X \times [t_0, t] \rightarrow R_x \times [t_0, t] \\ &(\boldsymbol{X}, t) \rightarrow \boldsymbol{\varphi}(\boldsymbol{X}, t) = (\boldsymbol{x}, t) \end{aligned} \tag{1}$$

which links $\boldsymbol{X}$ and $\boldsymbol{x}$ in time by the law of motion:

$$\boldsymbol{x} = \boldsymbol{x}(\boldsymbol{X}, t), \qquad t = t \tag{2}$$

It states that the spatial coordinates $\boldsymbol{x}$ depend both on the material particle, $\boldsymbol{X}$, and time t. Furthermore, physical time is measured by the same variable t in both material and spatial domains. For every fixed instant t, the mapping $\boldsymbol{\varphi}$ defines a configuration in the spatial domain. A matrix representation for the gradient $\boldsymbol{\varphi}$ is shown :

$$\frac{\partial \boldsymbol{\varphi}}{\partial (\boldsymbol{X}, t)} = \begin{pmatrix} \frac{\partial \boldsymbol{x}}{\partial \boldsymbol{X}} & \mathbf{v} \\ \mathbf{0}^{\mathrm{T}} & 1 \end{pmatrix} \tag{3}$$

e $\mathbf{0}^{\mathrm{T}}$ is a null row-vector and the material velocity $\mathbf{v}$ is represented by:

$$\mathbf{v}(\boldsymbol{X}, t) = \left.\frac{\partial \boldsymbol{x}}{\partial t}\right|_{\boldsymbol{X}} \tag{4}$$

e $|_{\boldsymbol{x}}$ means that the material coordinate $\boldsymbol{X}$ is fixed.
he referential domain R_χ is mapped into the material and spatial domains by $\boldsymbol{\Psi}$ and $\boldsymbol{\Phi}$, respectively, as n in Fig. 1. The particle motion $\boldsymbol{\varphi}$ can be expressed as $\boldsymbol{\varphi} = \boldsymbol{\Phi} \circ \boldsymbol{\Psi}^{-1}$, which indicates the dependence een the mappings $\boldsymbol{\varphi}$, $\boldsymbol{\Phi}$ and $\boldsymbol{\Psi}$.

The mapping of $\boldsymbol{\Phi}$ from the referential domain to the spatial domain, which can be considered as the motion of the mesh points in the spatial domain, is represented by:

$$\begin{aligned} &\boldsymbol{\Phi}: R_{\chi} \times [t_0, t] \rightarrow R_x \times [t_0, t] \\ &(\boldsymbol{\chi}, t) \rightarrow \boldsymbol{\Phi}(\boldsymbol{\chi}, t) = (\boldsymbol{x}, t) \end{aligned} \tag{5}$$

and the gradient of $\boldsymbol{\Phi}$ equals:

$$\frac{\partial \boldsymbol{\Phi}}{\partial (\boldsymbol{\chi}, t)} = \begin{pmatrix} \frac{\partial \boldsymbol{x}}{\partial \boldsymbol{\chi}} & \mathbf{w} \\ \mathbf{0}^{\mathrm{T}} & 1 \end{pmatrix} \tag{6}$$

where the mesh velocity $\mathbf{w}$ is defined by following relation:

$$\mathbf{w}(\boldsymbol{\chi}, t) = \left. \frac{\partial \boldsymbol{x}}{\partial t} \right|_{\boldsymbol{\chi}} \tag{7}$$

Both the material and the mesh move with respect to the spatial domain.

Further, considering $\boldsymbol{\Psi}$, it is suitable to be represented by inversion $\boldsymbol{\Psi}^{-1}$:

$$\begin{aligned} &\boldsymbol{\Psi}^{-1}: R_X \times [t_0, t] \rightarrow R_{\chi} \times [t_0, t] \\ &(\boldsymbol{X}, t) \rightarrow \boldsymbol{\Psi}^{-1}(\boldsymbol{X}, t) = (\boldsymbol{\chi}, t) \end{aligned} \tag{8}$$

and the gradient of $\boldsymbol{\Psi}^{-1}$ equals:

$$\frac{\partial \boldsymbol{\Psi}^{-1}}{\partial (\boldsymbol{X}, t)} = \begin{pmatrix} \frac{\partial \boldsymbol{\chi}}{\partial \boldsymbol{X}} & \mathbf{u} \\ \mathbf{0}^{\mathrm{T}} & 1 \end{pmatrix} \tag{9}$$

where the velocity $\mathbf{u}$ has the following form:

$$\mathbf{u}(\boldsymbol{X}, t) = \left. \frac{\partial \boldsymbol{\chi}}{\partial t} \right|_{\boldsymbol{X}} \tag{10}$$

and can be understood as the particle velocity in the referential domain.

The relations between velocities can be obtained by differentiating $\boldsymbol{\varphi} = \boldsymbol{\Phi} \circ \boldsymbol{\Psi}^{-1}$,

$$\frac{\partial \boldsymbol{\varphi}}{\partial (\boldsymbol{X}, t)}(\boldsymbol{X}, t) = \frac{\partial \boldsymbol{\Phi}}{\partial (\boldsymbol{\chi}, t)}\left(\boldsymbol{\Psi}^{-1}(\boldsymbol{X}, t)\right) \frac{\partial \boldsymbol{\Psi}^{-1}}{\partial (\boldsymbol{X}, t)}(\boldsymbol{X}, t) = \frac{\partial \boldsymbol{\Phi}}{\partial (\boldsymbol{\chi}, t)}(\boldsymbol{\chi}, t) \frac{\partial \boldsymbol{\Psi}^{-1}}{\partial (\boldsymbol{X}, t)}(\boldsymbol{X}, t) \tag{11}$$

or, in matrix form:

$$\begin{pmatrix} \frac{\partial \boldsymbol{x}}{\partial \boldsymbol{X}} & \mathbf{v} \\ \mathbf{0}^{\mathrm{T}} & 1 \end{pmatrix} = \begin{pmatrix} \frac{\partial \boldsymbol{x}}{\partial \boldsymbol{\chi}} & \mathbf{w} \\ \mathbf{0}^{\mathrm{T}} & 1 \end{pmatrix} \begin{pmatrix} \frac{\partial \boldsymbol{\chi}}{\partial \boldsymbol{X}} & \mathbf{u} \\ \mathbf{0}^{\mathrm{T}} & 1 \end{pmatrix} \tag{12}$$

which leads to the following relation:

$$\mathbf{v} = \mathbf{w} + \frac{\partial \boldsymbol{x}}{\partial \boldsymbol{\chi}} \cdot \mathbf{u} \tag{13}$$

quation above can be presented as follows:

$$\mathbf{c} := \mathbf{v} - \mathbf{w} = \frac{\partial \boldsymbol{x}}{\partial \boldsymbol{\chi}} \cdot \mathbf{u} \tag{14}$$

e $\mathbf{c}$ is defined as convective velocity that is the relative velocity between the material and the mesh.

et us note that the convective velocity $\mathbf{c}$ should not be mistaken with velocity $\mathbf{u}$, which is the particle ity as seen from the referential domain R_{χ}, while $\mathbf{c}$ is the particle velocity relative to the mesh as seen the spatial domain R_x. Actually, Eq. (14) indicates that $\mathbf{c} = \mathbf{u}$ then and only when $\partial \boldsymbol{x} / \partial \boldsymbol{\chi} = \mathbf{I}$ (where $\mathbf{I}$ Gibbs' idemfactor).

he freedom of moving the mesh helps one to combine the adequate qualities of the Lagrangian and ian formulations, by which the ALE formulation is very attractive.

2.2 Material, spatial and referential time derivatives in the arbitrary Lagrangian–Eulerian formulation.

A relations between material time derivative and referential time derivative are necessary to provide the conservation laws for mass, momentum and energy in the ALE formulation.

For the purpose of finding the relation of the time derivative in the material, spatial and referential domains, let a scalar physical quantity be described by functional forms: $f(\boldsymbol{X}, t)$, $f(\boldsymbol{x}, t)$ and $f(\boldsymbol{\chi}, t)$ in the material, spatial and referential domain, respectively.

Because the particle motion $\boldsymbol{\varphi}(\boldsymbol{X}, t)$ is a mapping, the material description $f(\boldsymbol{X}, t)$, and the spatial description $f(\boldsymbol{x}, t)$ of the physical quantity can be expressed as follows:

$$f(\boldsymbol{X}, t) = f(\boldsymbol{\varphi}(\boldsymbol{X}, t), t) \text{ or } f(\boldsymbol{X}, t) = f(\boldsymbol{x}, t) \circ \boldsymbol{\varphi}(\boldsymbol{X}, t). \tag{15}$$

The gradient of the above expression can be determined as:

$$\frac{\partial f}{\partial(\boldsymbol{X}, t)}(\boldsymbol{X}, t) = \frac{\partial f}{\partial(\boldsymbol{x}, t)}(\boldsymbol{x}, t) \frac{\partial \boldsymbol{\varphi}}{\partial(\boldsymbol{X}, t)}(\boldsymbol{X}, t) \tag{16}$$

which can be also written in the matrix form

$$\left(\frac{\partial f}{\partial \boldsymbol{X}} \frac{\partial f}{\partial t}\right) = \left(\frac{\partial f}{\partial \boldsymbol{x}} \frac{\partial f}{\partial t}\right) \begin{pmatrix} \frac{\partial \boldsymbol{x}}{\partial \boldsymbol{X}} & \mathbf{v} \\ \mathbf{0}^{\mathrm{T}} & 1 \end{pmatrix} \tag{17}$$

after block multiplication, two expressions were obtained in the following forms:

$$\frac{\partial f}{\partial \boldsymbol{X}} = \frac{\partial f}{\partial \boldsymbol{x}} \frac{\partial \boldsymbol{x}}{\partial \boldsymbol{X}} \tag{18}$$

$$\left.\frac{\partial f}{\partial t}\right|_{\boldsymbol{X}} = \left.\frac{\partial f}{\partial t}\right|_{\boldsymbol{x}} + \frac{\partial f}{\partial \boldsymbol{x}} \cdot \mathbf{v} \tag{19}$$

the second expression is the well-known equation that relates the material and the spatial time derivatives, which can also be written as:

$$\frac{\mathrm{d}f}{\mathrm{d}t} = \frac{\partial f}{\partial t} + \operatorname{div}(f\mathbf{v}) \tag{20}$$

In the following text, the referential time derivative is included to the relation between material and spatial time derivative.

The transformation from the referential description $f(\boldsymbol{\chi}, t)$ of the scalar physical quantity to the material description $f(\boldsymbol{X}, t)$ can be written as a result of mapping $\boldsymbol{\Psi}$ in the following form:

$$f(\boldsymbol{X}, t) = f(\boldsymbol{\chi}, t) \circ \boldsymbol{\Psi}^{-1} \tag{21}$$

whereas its gradient can be expressed as:

$$\frac{\partial f}{\partial(\boldsymbol{X}, t)}(\boldsymbol{X}, t) = \frac{\partial f}{\partial(\boldsymbol{\chi}, t)}(\boldsymbol{\chi}, t) \frac{\partial \boldsymbol{\Psi}^{-1}}{\partial(\boldsymbol{X}, t)}(\boldsymbol{X}, t) \tag{22}$$

ı can be also written in matrix form:

$$\left(\frac{\partial f}{\partial \boldsymbol{X}} \frac{\partial f}{\partial t}\right) = \left(\frac{\partial f}{\partial \boldsymbol{\chi}} \frac{\partial f}{\partial t}\right) \begin{pmatrix} \frac{\partial \boldsymbol{\chi}}{\partial \boldsymbol{X}} & \mathbf{u} \\ \mathbf{0}^{\mathrm{T}} & 1 \end{pmatrix} \tag{23}$$

block multiplication, two expressions were obtained in the following forms:

$$\frac{\partial f}{\partial \boldsymbol{X}} = \frac{\partial f}{\partial \boldsymbol{\chi}} \frac{\partial \boldsymbol{\chi}}{\partial \boldsymbol{X}} \tag{24}$$

$$\left.\frac{\partial f}{\partial t}\right|_{\boldsymbol{X}} = \left.\frac{\partial f}{\partial t}\right|_{\boldsymbol{\chi}} + \frac{\partial f}{\partial \boldsymbol{\chi}} \cdot \mathbf{u} \tag{25}$$

The equation above relates the material and the referential time derivatives. However, it requires the evaluation of the gradient of the considered quantity in the referential domain which is more difficult for computational mechanics than to work in the spatial domain. Furthermore, constitutive relations are stated in the spatial configuration in fluids. Hence, by means of Eq. (14), the previous equation can be converted into:

$$\left.\frac{\partial f}{\partial t}\right|_{\boldsymbol{X}} = \left.\frac{\partial f}{\partial t}\right|_{\boldsymbol{\chi}} + \frac{\partial f}{\partial \boldsymbol{x}} \cdot \mathbf{c} \text{ or } \left.\frac{\partial f}{\partial t}\right|_{\boldsymbol{X}} = \left.\frac{\partial f}{\partial t}\right|_{\boldsymbol{\chi}} + \operatorname{div}(f\mathbf{c}) \tag{26}$$

The equation above expresses the fundamental ALE relations between material time derivatives, referential time derivatives and spatial gradient and shows that the time derivative of the physical quantity f for a given particle $\boldsymbol{X}$ is its local derivative (with the reference coordinate $\boldsymbol{\chi}$ held fixed) plus a convective term taking into account the relative velocity $\mathbf{c}$ between the material and the reference system.

2.3 The arbitrary Lagrangian–Eulerian form of the balance equations

The ALE forms of the balance equations for mass, momentum and energy are established in this section. The set of the balance equations for the ALE description is obtained from the well-known form in Eulerian description [22,23]:

$$\frac{\partial}{\partial t}\begin{Bmatrix}\rho\\ \rho\mathbf{v}\\ \rho e\end{Bmatrix} + \operatorname{div}\begin{Bmatrix}\rho\mathbf{v}\\ \rho\mathbf{v}\otimes\mathbf{v}\\ \rho e\mathbf{v}\end{Bmatrix} = \operatorname{div}\begin{Bmatrix}0\\ \mathbf{t}\\ \mathbf{t}\mathbf{v}+\mathbf{q}\end{Bmatrix} + \begin{Bmatrix}0\\ \rho\mathbf{b}\\ \rho\mathbf{b}\mathbf{v}\end{Bmatrix} \tag{27}$$

where ρ is the density of the continuum particle, $\mathbf{v}$ velocity of the continuum particle, $e = c_v T + \frac{1}{2}\mathbf{v}^2$ total energy, c_v is specific heat at constant volume, T is temperature of the continuum particle, $\mathbf{t}$ the Cauchy stress flux, $\mathbf{q} = \lambda \cdot T\nabla$ the molecular heat flux defined by Fourier law (λ is thermal conductivity coefficient), $\mathbf{b}$ earth acceleration. The Cauchy stress flux can be divided into an elastic part and a diffusive part:

$$\mathbf{t} = \mathbf{P} + \boldsymbol{\tau}^c \tag{28}$$

where $\mathbf{P}$ is an elastic momentum flux which is reversible and $\boldsymbol{\tau}^c$ is a total diffusive momentum flux which describes irreversible phenomena.

The elastic part $\mathbf{P}$ is the spherical pressure tensor in the case of liquids, which cannot transmit the elastic shear stress. In the case of solids, $\mathbf{P}$ has the full form of the elastic stress tensor [22]:

$$\mathbf{P} = \begin{cases} -p\mathbf{I} = -p\delta_{ij}\mathbf{e}_i \otimes \mathbf{e}_j & -fluid \\ \boldsymbol{\sigma} = \sigma_{ij}\mathbf{e}_i \otimes \mathbf{e}_j & -solid \end{cases} \tag{29}$$

where p represents a thermodynamical pressure. The minus sign in the case of a fluid is due to the fact that the elastic momentum flux is the pressure directed towards the centre of the particle and compressing the substance.

The total diffusive momentum flux is defined in the following form:

$$\boldsymbol{\tau}^c = \boldsymbol{\tau} + \mathbf{R} + \mathbf{D} + \cdots \tag{30}$$

e $\boldsymbol{\tau}$ is a viscous momentum flux, $\mathbf{R}$ is a turbulent momentum flux, $\mathbf{D}$ is a diffusion momentum flux, "..." sents other fluxes that have been neglected in these considerations, e.g. transpirational momentum flux. he viscous momentum flux is given by the following equation:

$$\boldsymbol{\tau} = -\frac{2}{3}\mu I_{\mathbf{d}}\mathbf{I} + 2\mu\mathbf{d} \tag{31}$$

e μ is the molecular viscosity, $I_{\mathbf{d}} = \operatorname{tr}\mathbf{d}$ is the first invariant of the strain rate, $\mathbf{d} = \frac{1}{2}(\mathbf{v}\otimes\nabla + \nabla\otimes\mathbf{v})$ is train rate tensor.

he turbulent momentum flux $\mathbf{R}$ also known as turbulent Reynolds stress can be written as an analogy to ewtonian fluid model:

$$\mathbf{R} = -\frac{2}{3}\mu_t I_{\mathbf{d}}\mathbf{I} + 2\mu_t\mathbf{d} \tag{32}$$

Fig. 2 A general view of the wind tunnel

where μ_t is the turbulent viscosity coefficient. In what follows we consider in (30) $\boldsymbol{\tau}$ and $\mathbf{R}$ only.

From the considerations of the previous section it can be concluded that it is necessary to replace the velocity $\mathbf{v}$ with the relative velocity $\mathbf{c}$ in the convective part of the equations of the balance, in order to obtain the ALE formulation of the equations of the balance [20]. The set of the ALE balance equations can be expressed in the following form:

$$\frac{\partial}{\partial t}\begin{Bmatrix}\rho\\ \rho\mathbf{v}\\ \rho e\end{Bmatrix}+\operatorname{div}\begin{Bmatrix}\rho\mathbf{c}\\ \rho\mathbf{v}\otimes\mathbf{c}\\ \rho e\mathbf{c}\end{Bmatrix}=\operatorname{div}\begin{Bmatrix}0\\ \mathbf{t}\\ \mathbf{tv}+\mathbf{q}\end{Bmatrix}+\begin{Bmatrix}0\\ \rho\mathbf{b}\\ \rho\mathbf{bv}\end{Bmatrix} \tag{33}$$

which can be expressed also as:

$$\frac{\partial}{\partial t}\begin{Bmatrix}\rho\\ \rho\mathbf{v}\\ \rho e\end{Bmatrix}+\operatorname{div}\begin{Bmatrix}\rho(\mathbf{v}-\mathbf{w})\\ \rho\mathbf{v}\otimes(\mathbf{v}-\mathbf{w})\\ \rho e(\mathbf{v}-\mathbf{w})\end{Bmatrix}=\operatorname{div}\begin{Bmatrix}0\\ \mathbf{t}\\ \mathbf{tv}+\mathbf{q}\end{Bmatrix}+\begin{Bmatrix}0\\ \rho\mathbf{b}\\ \rho\mathbf{bv}\end{Bmatrix} \tag{34}$$

3 Experiment on the flow over a thin platelet

An experiment was prepared to show the interaction between the fluid and the thin platelet in order to assess the reliability of the numerical model. The results of the experiment provide a basis for verification of models used in computational codes in both linear and nonlinear ranges, for mutual couplings of CDF and CSD codes. The thin rectangular platelet was placed in a wind tunnel (Fig. 2) in a nozzle with a rectangular cross section and perpendicular to the direction of flow (Fig. 3). The wind tunnel in Göttingen is capable of being changed independently Mach number and Reynolds number. The flow field for calibrating probes is well suited at subsonic Mach numbers and at supersonic Mach numbers [24]. At the set thickness and height of the plate and flow velocity, the plate began to deform and then vibrate. The aim of the measurement was to measure the amplitude and frequency of vibrations and to investigate the instability of flow in the vicinity of the tested
et. Air stream velocity was from 0.3 to 0.9 Ma. Flow characteristics have been measured by a quantitative
ren method, and the vibration frequency of the plate have been measured using a photodiode connected
oscilloscope.
he platelet is seated between two fixed rigidly screwed plates. The general view of the platelet is shown
. 4. In the wind tunnel there is only the upper part of the platelet with dimensions 30×24 mm. The width
wider part of the platelet is 30 mm, and the narrower part is 20 mm. The total height of the platelet is
m, but the wider part of the platelet is 50 mm in height and the narrower part is 30 mm (Fig. 4).
he platelet is made of 0.2 mm thick structural steel. Its material properties are given in Table 1 below.
mplitude and natural frequency of the platelet have been measured (Fig. 5). Amplitude means the incli-
n of the upper surface of the platelet from the vertical. Afterwards, the results have been subjected to the
er analysis, which is depicted in Fig. 6.
he plate is bent by the force of the aerodynamic drag and bend it as the flow rate increases. In this case
ave stationary bending of the plate and non-stationary vibrations of the free plate end. The measured

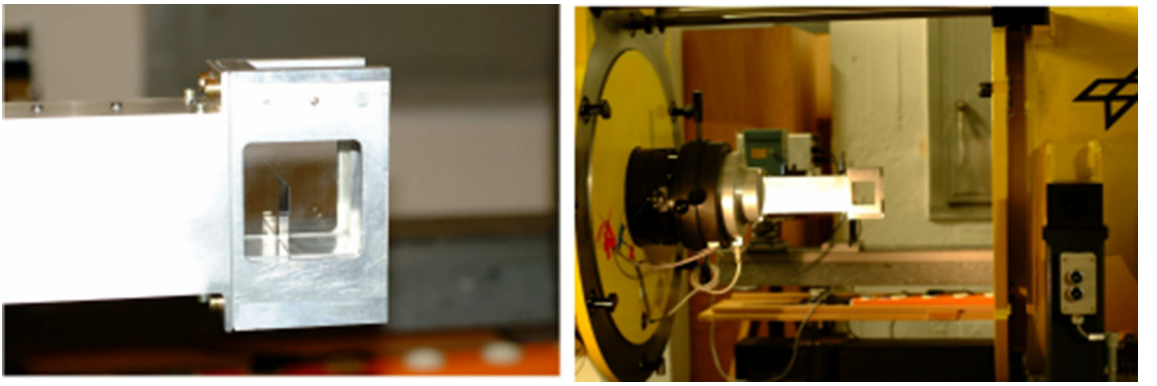

Fig. 3 The rectangular nozzle with the platelet

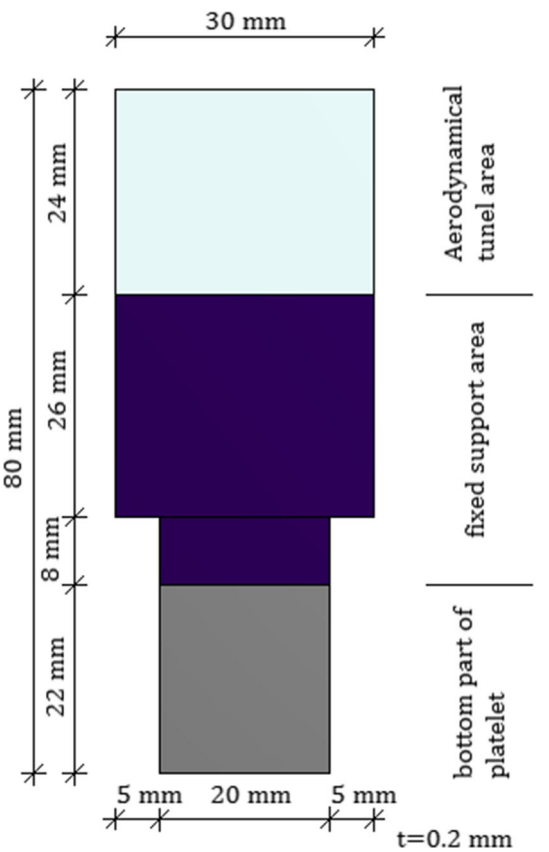

The general view and dimensions of the platelet

1 Assumed steel properties

sity	7860	(kg/m^3)
ng modulus	210	(GPa)
son's ratio	0.3	(–)
ffient of thermal expansion	1.2e−05	(1/°C)

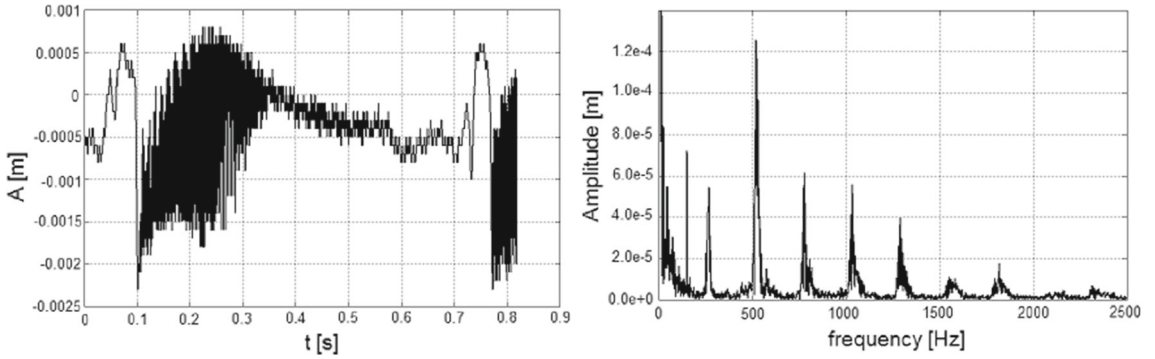

Fig. 5 Amplitude and natural frequency of the platelet with 0.2 mm thickness

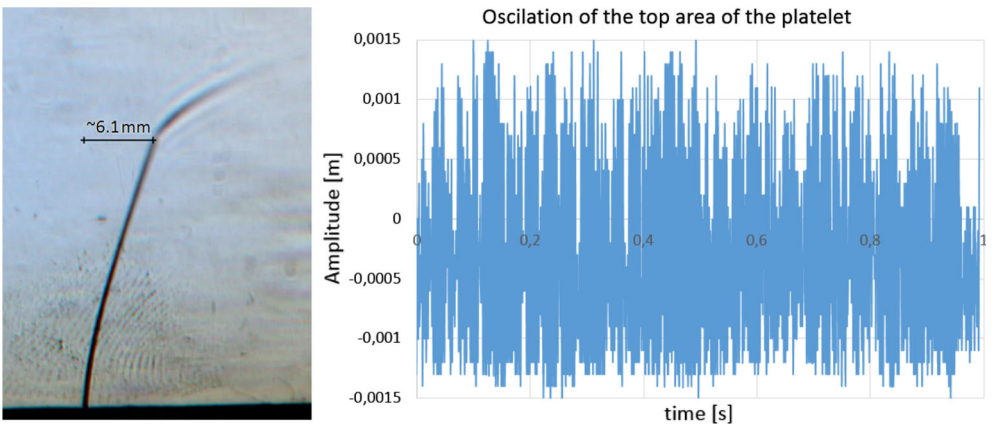

Fig. 6 Deflection of the 0.2 mm platelet for 0.7 Ma (left) and amplitude of platelet oscillation (right) for time range 1 s

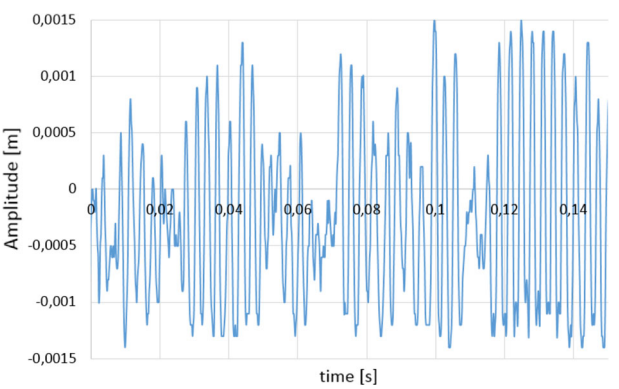

Amplitude of platelet oscillation (right) for time range 0.15 s

ıation of the platelet was approximately 6.1 mm (Fig. 6 left part). Obviously, due to the non-stationary the deflection was constantly oscillating around this value with a variable amplitude of max 1.5 mm. The ured total time of the oscillation was 1 s, with the measurement every 0.0002 s (Fig. 6 right part).

ue to the poor visibility of oscillations in Figs. 6 and 7 shows the measured oscillations in a smaller time ral, namely between 0 and 0.15 s, so that the nature of the motion of the plate under the influence of w can be determined more accurately.

gure 7 shows the amplification and decay of the plate oscillation amplitude, which is characteristic of is known as beating [25]. The character of the plate motion results from the overlapping of the imposing , i.e. the air flow pressure and the forces resisting the flow, i.e. the inertia force and the elastic force, which ermined by the flexural and torsional stiffness of the plate.

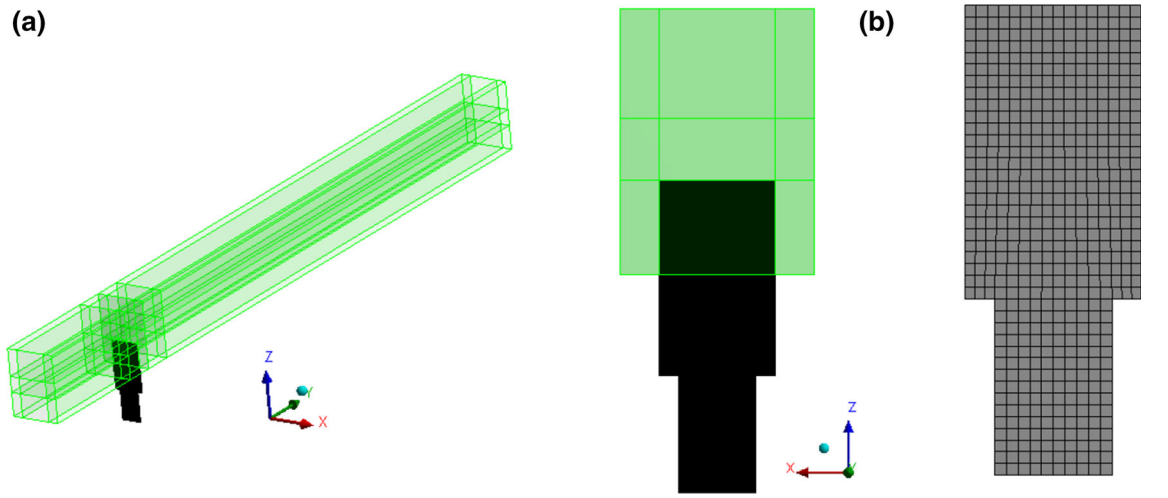

Fig. 8 **a** Geometry of the numerical domains and **b** discretization domain of the solid body domain (550 elements, 4133 nodes)

Vortex structures which are quite stable in the flow are responsible for the vibrations of the plate bent by the flow. The frequency of these vibrations changes with the increase of the Mach number, but the change is insignificant.

4 Numerical investigation

The partitioned approach [26–30] is used to couple the characteristics of the solid and of the fluid in the FSI Analysis. In the partitioned approach analysis task is divided into three sub-tasks: the fluid, the solid, the mesh. Flow equations are solved by CFD solver, and the response of the solid body is obtained by using CSD solver. In the case of the following study, the CFD solver is based on the finite volume method [23,31] and the CSD is based on the finite element method [32].

The finite volume method is a numerical method allowing solution of differential partial equations in the form of algebraic equations and it is one of the basic methods used in CFD computations. The surface integrals in the finite volume are solved. Discretization of the model is easy to generate even for complex shapes in this method [23]. The finite element method is a numerical approximation technique solving complicated differential equations (Partial Differential Equations—PDE). The FEM approach is based on the elimination of spatial derivatives from partial differential equations and replacing them with a large number of algebraic equations. In mathematical terms, it is an extension and improvement in Rayleigh-Ritz and Galerkin method [32].

As mentioned before, the solid and the fluid domains are computed in separate codes using different methods. ALE formulations are obtained by ensuring balance between the forces responsible for interactions between fluid and solids domains (momentum balance from Eq. (34) between solid and fluid domains) and the equality in deformations between these domains provided by the boundary condition at the interface of these domains [12]:

$$\mathbf{w}|_{solid} = \mathbf{w}|_{fluid} \tag{35}$$

where: $\mathbf{w}|_{solid}$ is the mesh velocity of the solid domain, $\mathbf{w}|_{fluid}$ is the mesh velocity of the fluid domain. Also ALE formulations were obtained through a moving grid in CFD solver and its movement is described by the Laplace equation [12]:

$$\operatorname{div}\left(\operatorname{grad}\mathbf{w}|_{fluid}\right) = \mathbf{0} \tag{36}$$

The model contains a fluid part (which represent wind tunnel)—air with ideal gas properties and a solid part representing a platelet (Table 1. Platelet steel properties). The model geometry is presented in Fig. 8. A lack of material nonlinearities is assumed in the platelet model; however, geometrical nonlinearities occur.

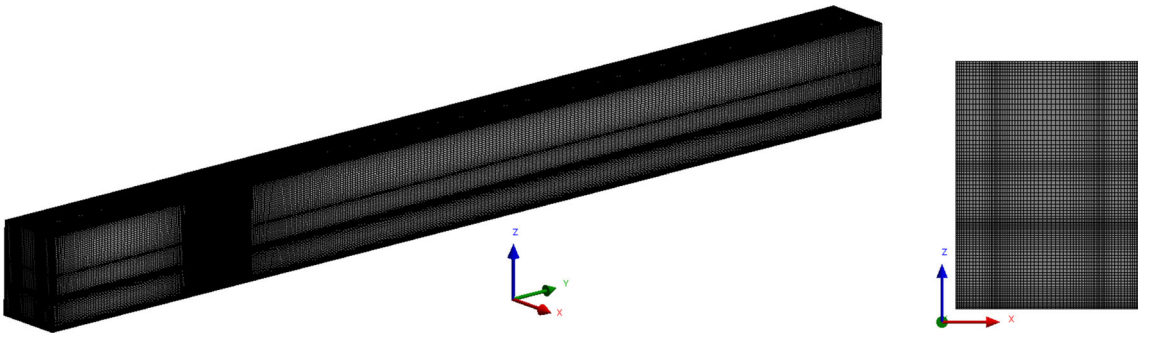

Fig. 9 Discretization of the fluid domain (2,533,100 volumes, 2,607,262 nodes)

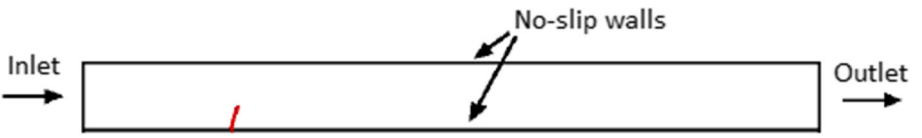

Fig. 10 Boundary conditions assigned in the model

The platelet was divided into 550 finite elements (20-noded hexahedral elements), see Fig. 9. The air domain was divided into 2,533,100 finite volumes (8-noded hexahedral volumes). The standard semi-implicit method for pressure-linked equations (SIMPLE) method has been used for pressure–velocity coupling. The second-order upwind schemes have been used for obtaining the solution of the convection term in governing equations. The diffusion terms have been central-differenced with the second-order accuracy as well. The detailed methodology of numerical integration regarding the set of governing equations can be found in [23,31]. The turbulence was modelled using the Spalart–Allmaras model [33].

The following boundary conditions are assigned in the fluid part of the model (Fig. 10). The velocity of the air stream on the external surface of the platelet equals zero, as in [23] and is a typical condition applied at a wall. Pressure-inlet and pressure-outlet are correspondingly assigned to surfaces at the inlet and outlet of the domain. The lateral edges of the domain are treated as wall with no-slip conditions. In order to simplify the simulation, it is assumed that the upstream velocity is constant and uniform.

Boundary conditions for a case with Mach number 0.7 were as follows: Inlet—air was drawn from the environment, inlet pressure equal to 101,325 Pa, a value of temperature was 298.15 K, the direction of velocity was set perpendicular to the inlet. The outlet in experiment was a container with reduced pressure to a value resulting in a flow with a speed of 0.7 Mach in case of absence of the plate in the wind tunnel. Static pressure at the outlet was equal to 73,048 Pa. The platelet was fixed as shown in Fig. 4.

Figure 11 shows the deflection of the plate due to wind tunnel flow, which is a maximum of 6.26 mm. Two projections are presented. The first one is the side view, which was later compared with the experimental photo, and the second one shows the inclination of the platelet more generally. The figure shows only the part of the platelet in the wind tunnel.

ı order to obtain a numerical simulation of the platelet inclination in agreement with the experiment, g Modulus had to be increased to 210 GPa, because simulations with Young Modulus from Table 1 ed in significantly overestimated displacements.

igure 12 shows a comparison of the results of aeromechanical calculations with a photograph taken during speriment. It shows a very good agreement on the results of numerical faces with the experiment; the ge inclination of the platelet in both cases is almost the same. The following figures (Figs. 13, 14) give erview of the flow that has been obtained from the described FSI simulation.

igure 12 shows a photo taken with the Schlieren technique in the platelet extension, in fact above it there ongitudinal shadow. Results of numerical simulations, presented Figs. 13 and 14, show clearly that this trace of the friction layer that forms the boundary between the flow from the platelet and the separation ed behind the plate. This friction layer is related to the change in density, which is visualized by the optical od. Significant role of compressibility in the flows studied here results from the high velocities obtained nozzle.

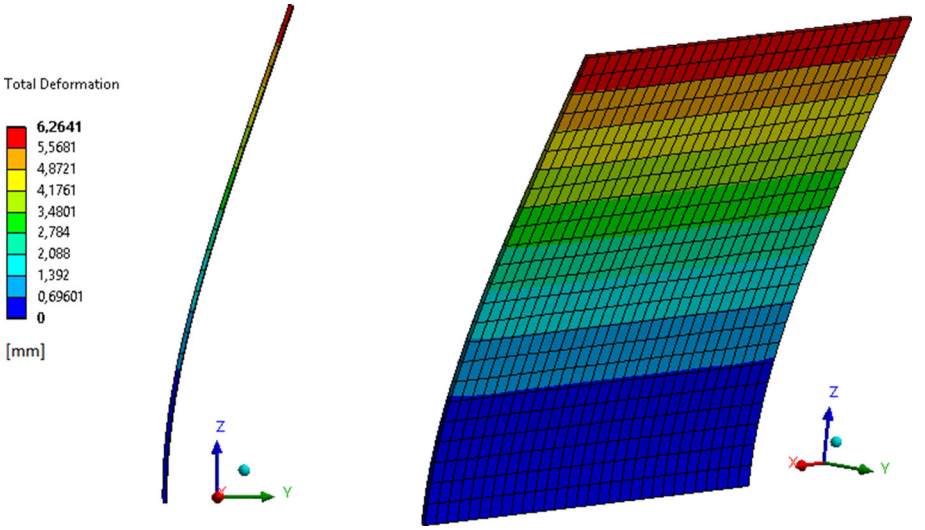

Fig. 11 Deflection of the platelet in the aerodynamical tunnel area using finite strain analysis

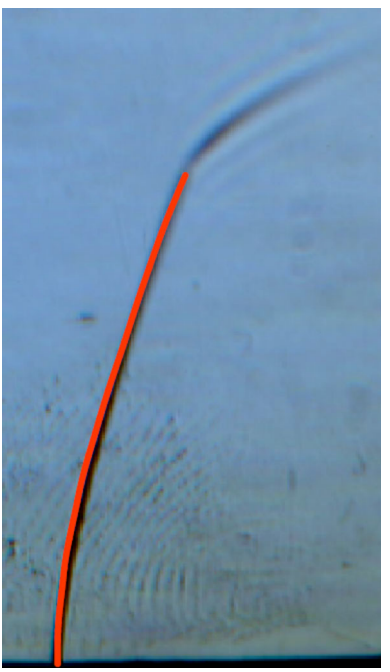

Fig. 12 Overlaying the deflection view of the plate during the experiment and the result of the simulation for velocity 0.7 Ma

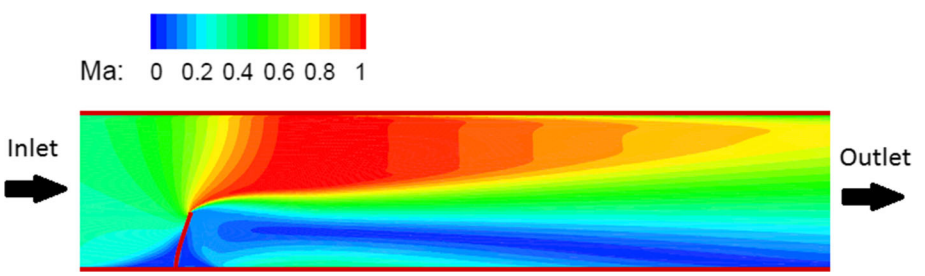

3 Results of aeromechanical calculations of platelet in flow—Mach number distribution

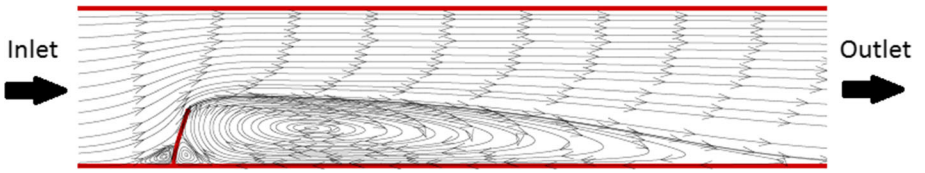

Fig. 14 Results of aeromechanical calculations of the plate in the flow—the stream lines

As shown in Fig. 13, the Mach number greater than 1 is obtained in the throat of the nozzle. Therefore, in the case under consideration, the nozzle works as a critical nozzle.

Further work to be carried out should focus on the attempt at correct representation of the nature of the flow. Only when a transient flow is achieved will it be possible to a full analysis of the problem. This will be a big challenge due to the numerical difficulty of the type of flow considered here.

5 Summary

The paper compares the experimental analysis of a flow disturbed by an elastic thin plate in a wind tunnel with numerical calculations using FSI tools modified using arbitrary Lagrangian–Eulerian approach. In the experiments, it has been investigated the instability of flow in the vicinity of the tested platelet. The amplitude and frequency of vibrations of the platelet were measured as a function of Mach number and a given pressure, the character of the flow before and after the platelet was examined. Additionally, the following natural frequencies were measured. The amplification and decay of the plate oscillation amplitude were observed, which can be interpreted as a beating phenomenon. In the investigated case, we have stationary deflection of the plate and non-stationary vibrations of its free end. Vortex structures that are quite stable in the flow are responsible for the vibrations of the platelet curved by the flow.

Despite the large nonlinear deformations, the plate was not damaged. The inclination of the plate was 6.1 mm, which at the height of the part of the plate located in the wind tunnel, and equal to 24 mm, causes this phenomenon be strongly nonlinear. The adoption of the elastic and isotropic material in the model and the treatment of nonlinearity only by analysis of finite deformations proved to be insufficient due to the later need to increase the Young's module. However, after this treatment, the results of the deflections for the case under consideration were very consistent.

In the case under consideration we have a critical nozzle, because obtained the Mach numbers were greater than one. High nozzle speeds caused that changes in air density played an important role in the analysis.

Acknowledgements VAE acknowledges the support of the Ministry of Education and Science of the Russian Federation, Project No. 9.1001.2017/4.6.

References

1. WMO: Beaufort Scale of Wind Force (Technical and operational aspects). Commission for Marine Meteorology. Report on Marine Science Affairs No. 3, 22 pp. Geneva: WMO (1970)
orenc, H.: Structure of maximum wind velocities in Poland. In: Lorenc, H. (ed.) Natural Disasters in Relation to the Country's ternal Security (in polish). Institute of Meteorology and Water Management - National Research Institute, Warsaw (2012)
ukowski, J.: Fluid Mechanics (in Polish). PWN, Warsaw (1959)
obczyk, B., Chróścielewski, J., Witkowski, W.: Wind induced vibration analysis of composite footbridge. Biuletyn WAT (1), 91–101 (2015). (In Polish)
iółkowski, P.J., Sobczyk, B., Witkowski, W.: Analysis of unsteady forces acting on a slender cylinder. TFFM **140**, 23–38 018)
anas, K., Badur, J.: Influence of strength differential effect on material effort of a turbine guide vane based on thermoe- stoplastic analysis. J. Therm. Stress. **40**(11), 1368–1385 (2017)
adur, J., Bryk, M., Ziółkowski, P., Sławinski, D., Ziółkowski, P.J., Kornet, S., Stajnke, M.: On a comparison of Huber– lises–Hencky with Burzynski–Pecherski equivalent stresses for glass body during nonstationary thermal load. AIP Conf. oc. **1822**, 020002 (2017)
adur, J., et al.: Analysis of unsteady flow forces acting on the thermowell in a steam turbine control stage. J. Phys. Conf. er. **760**, 012001 (2016)
raszewski, B., Bzymek, G., Ziółkowski, P., Badur, J.: Extremal thermal loading of a bifurcation pipe. AIP Conf. Proc. **2077**, 20030 (2019)

10. Bielecki, M., Karcz, M., Radulski, W., Badur, J.: Thermo-mechanical coupling between the flow of steam and deformation of the valve during start-up of the 200 MW turbine. Task Q. **5**(2), 125–140 (2001)
11. Ochrymiuk, T.: Numerical analysis of microholes film/effusion cooling effectiveness. J. Therm. Sci. **25**(5), 459–464 (2017)
12. Czechowicz, K., Badur, J., Narkiewicz, K.: Two-way FSI modeling of blood flow through CCA accounting on-line medical diagnostics in hypertension. J. Phys. Conf. Ser. **530**, 012011 (2014)
13. Badur, J., et al.: Enhanced energy conversion as a result of fluid–solid interaction In micro- and nanos cale. J. Theor. Appl. Mech. **56**, 329–332 (2018)
14. Badur, J., Karcz, M., Lemanski, M.: On the mass and momentum transport in the Navier-Stokes slip layer. Microfluid. Nanofluid. **11**, 439–449 (2011)
15. Ziółkowski, P., Badur, J.: A theoretical, numerical and experimental verification of the Reynolds thermal transpiration law. Int. J. Numer. Methods Heat Fluid Flow **28**(1), 64–80 (2018)
16. Badur, J., Ziólkowski, P.J., Ziólkowski, P.: On the angular velocity slip in nano flows. Microfluid. Nanofluid. **19**(1), 191–198 (2015)
17. Kowalewski, T.A., et al.: Micro and nano fluid mechanics. In: Kleiber, M., et al. (eds.) Advances in Mechanics: Theoretical, Computational and Interdisciplinary Issues. Taylor & Francis Group, London (2016)
18. Lewandowski, T., Ochrymiuk, T., Czerwinska, J.: Modeling of heat transfer In micro channel gas flow. ASME J. Heat Transf. **133**(2), 022401 (2011)
19. Ziółkowski, P., Badur, J.: Navier number and transition turbulencje. J. Phys. Conf. Ser. **530**, 012035 (2014)
20. Donea, J., Huerta, A., Ponthot, J.-P., Rodrigez-Ferran, A.: Chapter 14: Arbitrary Lagrangian–Eulerian methods. In: Stein, E., de Borst, R., Hughes, J.R. (eds.) Encyclopedia of Computational Mechanics. Fundamentals, vol. 1. Wiley, New York (2004)
21. Margolin, L.G.: Introduction to "An Arbitrary Lagrangian-Eulerian Computing Method for All Flow Speeds". J. Comput. Phys. **135**, 198–202 (1997)
22. Badur, J.: Five Lectures on Contemporary Fluid Thermomechanics. IFFM, Gdańsk (2005)
23. Hirsch, C.: Numerical Computation of Internal Andexternal Flows. Fundamentals of Computational Fluid Dynamics, vol. 1. Elsevier, Amsterdam (2007)
24. Gieß, P.-A., Rehder, H.-J., Kost, F.: A new test facility for probe calibration—Offering independent variation of Mach and Reynolds number. In: Proceedings of the XVth Bi-annual symposium on measuring techniques in transonic and supersonic flow in cascades and turbomachines, Firenze September 21–22 (2000)
25. Skorko, M.: Physics. PWN, Warszawa (1978). (in Polish)
26. Hou, G., Wang, J., Layton, A.: Numerical methods for fluid-structure interaction–a review. Commun. Comput. Phys. **12**(2), 339–377 (2012)
27. Piperno, S., Farhat, C., Larrouturou, B.: Partitioned procedures for the transient solution of coupled aeroelastic problems. Part I: model problem, thory and two dimensional application. Comput. Methods Appl. Mech. Eng. **124**, 79–112 (1995)
28. Farhat, C., Lesoinne, M., Maman, N.: Mixed explicit/implicit time integration of coupled aeroelastic problems: there-field formulation, geometric conservation and distributed solution. Int. J. Numer. Methods Fluids **21**, 807–835 (1995)
29. Fahrat, C., Lesoinne, M.: Two efficient staggered algorithms for the serial and parallel solution of three-dimensional nonlinear transient aeroelastic problems. Comput. Methods Appl. Mech. Eng. **182**, 499–515 (2000)
30. Fahrat, C., Van der Zee, K.G., Geuzaine, P.: Provably second-order time accurate loosely-coupled solution algorithms for transient nonlinear computational aeroelasticity. Comput. Methods Appl. Mech. Eng. **195**, 1973–2001 (2006)
31. Badur, J.: Numerical modeling of Sustainable Combustion in Gas Turbines. IFFM Publishers, Gdańsk (2003)
32. Zienkiewicz, O.C.: Finite Element Method, vol. 1-3. Elsevier, Amsterdam (2005)
33. Spalart, P.R., Allmaras, S.R.: A one equation model for aerodynamics flows. La Rech. Aerosp. **1**, 5–21 (1994)